ACS central science

http://pubs.acs.org/journal/acscii

Research Article

Azo-Enhanced Raman Scattering for Enhancing the Sensitivity and Tuning the Frequency of Molecular Vibrations

Yuchen Tang,* Yongpeng Zhuang, Shaohua Zhang, Zachary J. Smith, Yuee Li, Xijiao Mu, Mengna Li, Caili He, Xingxing Zheng, Fangfang Pan, Tingjuan Gao,* and Lizhi Zhang

Cite This: *ACS Cent. Sci.* 2021, 7, 768–780

Read Online

ACCESS | Metrics & More | Article Recommendations | Supporting Information

ABSTRACT: Raman scattering provides stable narrow-banded signals that potentially allow for multicolor microscopic imaging. The major obstacle for the applications of Raman spectroscopy and microscopy is the small cross section of Raman scattering that results in low sensitivity. Here, we report a new concept of azo-enhanced Raman scattering (AERS) by designing the intrinsic molecular structures using resonance Raman and concomitant fluorescence quenching strategies. Based on the selection of vibrational modes and the enhancing unit of azobenzenes, we obtained a library of AERS molecules with specific Raman signals in the fingerprint and silent frequency regions. The spectral characterization and molecular simulation revealed that the azobenzene unit conjugated to the vibrational modes significantly enhanced Raman signals due to the mechanism of extending the conjugation system, coupling the electronic−vibrational transitions, and improving the symmetry of vibrational modes. The nonradiative decay of azobenzene from the excited state quenched the commitment fluorescence, thus providing a clean background for identifying Raman scattering. The most sensitive AERS molecules produced Raman signals of more than 4 orders of magnitude compared to 5-ethynyl-2′-deoxyuridine (EdU). In addition, a frequency tunability of 10 distinct Raman bands was achieved by selecting different types of vibrational modes. This methodology of AERS allows for designing small-molecule Raman probes to visualize various entities in complex systems by multicolor spontaneous Raman imaging. It will open new prospects to explore innovative applications of AERS in interdisciplinary research fields.

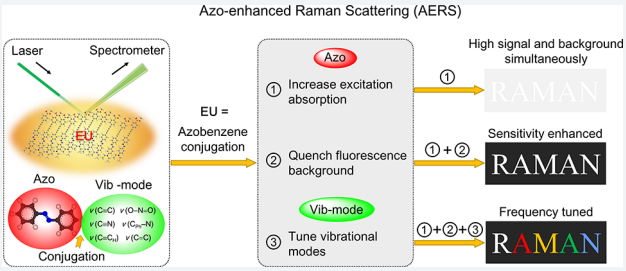

INTRODUCTION

The intrinsic nature of molecular vibrations enables narrow bands and stable intensities of Raman scattering when the vibrations are coupled with incident light. This feature provides a significant advantage for multicolor microscopic imaging and supercapacity information encoding using Raman scattering.[1−6] However, the low cross section of Raman scattering places one of the major obstacles when Raman spectroscopy and imaging are applied to identify trace amounts of components in complicated systems that require ultrasensitive detection, e.g., live cells.[7−11] Many strategies and techniques, such as coherent anti-Stokes Raman scattering (CARS), stimulated Raman scattering (SRS), surface-enhanced Raman scattering (SERS), and tip-enhanced Raman scattering (TERS), have been developed to boost Raman signals of molecules. Nonlinear optical methods such as CARS and SRS allow for high sensitivity, but the essential high-end lasers and sophisticated optics are typically not accessible for researchers to work with.[12−19] SERS and TERS offer potential signals with remarkable sensitivity and multiplicity, but the utility of plasmonic nanomaterials is undermined due to the difficulty of precisely controlling their dimension and/or location.[20−33]

Based on the comparison among different existing strategies, it can be found that the key enhancing units to boost Raman signals are extrinsic methodologies, e.g., nonlinear optical systems or plasmonic cavity. Besides these well-known strategies, molecules with inherent intense Raman scattering have been in large demand for a long time in order to enable facile Raman spectroscopy and imaging. This type of intrinsic enhancing strategy can be utilized alone to detect spontaneous Raman scattering or be compatible with the extrinsic enhancing methods as an additional amplifier.

Since the initial demonstration of cellular Raman imaging based on 5-ethynyl-2′-deoxyuridine (EdU),[34] numerous alkyne-containing molecules have been exploited to provide strong Raman signals.[35−40] The improved structures of phenyl-capped or polydiacetylene-based polyynes were synthesized for SRS imaging, while the former ones were demonstrated as

Received: January 23, 2021
Published: April 27, 2021

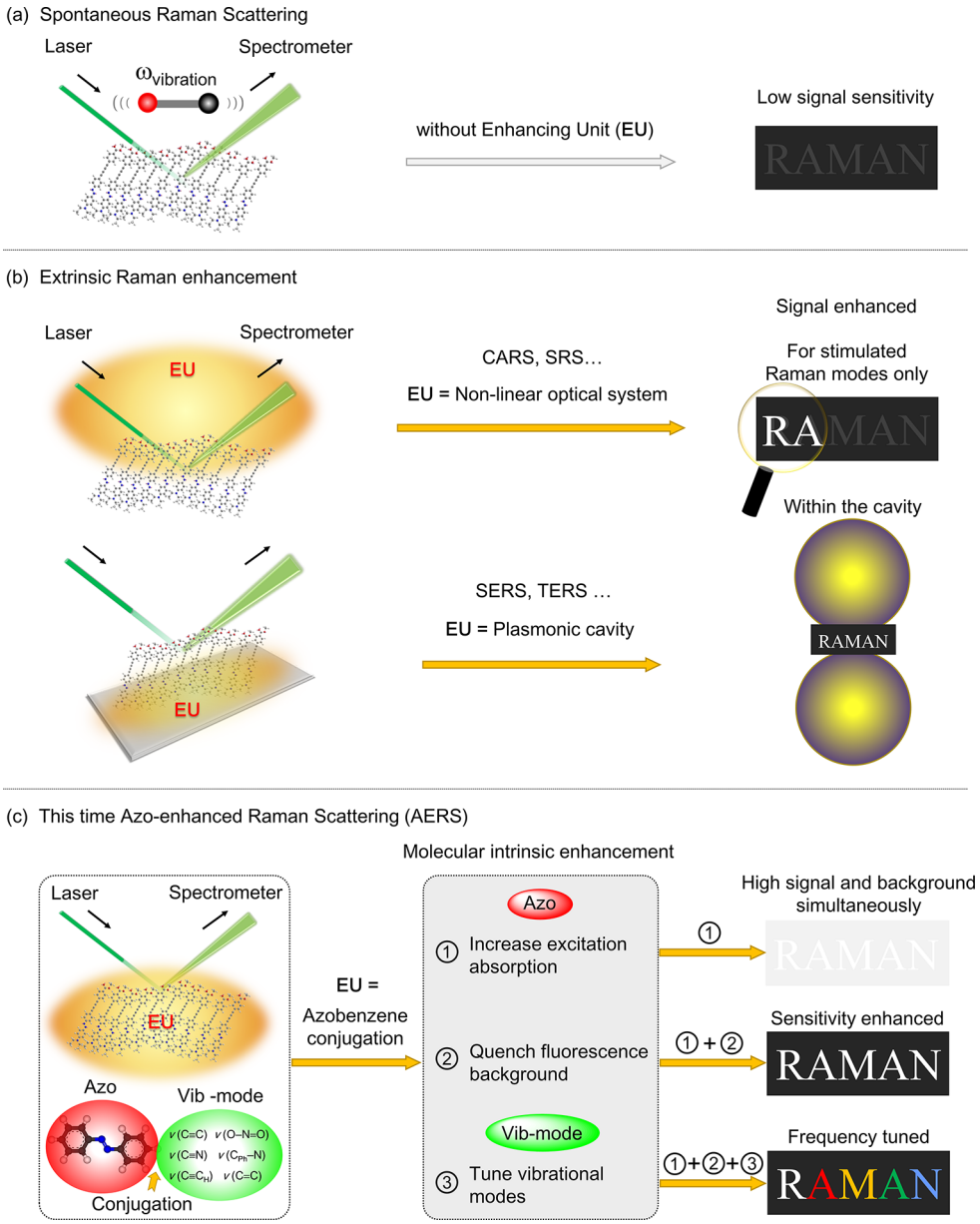

Figure 1. Concept of azo-enhanced Raman scattering (AERS).

tunable multicolor reporters.[4,5,17,41] However, the Raman intensity of C≡C stretching does not fulfill the sensitivity demand, especially when high quality of Raman imaging is required using spontaneous Raman microscopy. Researchers also demonstrated enhanced Raman signals using resonance Raman strategy that couples electronic and vibrational transitions through chromophores.[41−44] However, the capability of tuning Raman frequency was not achieved. Therefore, the current research lacks a general and systematic intrinsic strategy to enhance Raman signals for various vibrational modes in a large frequency range.

The fundamental bottleneck to achieve this goal was the discovery of the intrinsic building block to enhance a molecule's characteristic vibrational modes. This enhancing unit can be a chromophore that couples electronic and vibrational transitions. However, the key point is to enhance Raman intensity through the resonance Raman effect and simultaneously suppress the concurrent fluorescence caused by the chromophore absorption. Azo compounds have unique properties of tunable UV/vis absorbance and nonradiative de-excitations of the electronic states.[45−47] The intramolecular *cis/trans* structure change has been widely applied to study photoconversion processes.[48−50] Inspired by the findings, we demonstrate here a new concept of azo-enhanced Raman scattering (AERS, Figure 1). Conjugated azobenzene structures are the enhancing unit to boost Raman signals of various vibrational modes. This intrinsic molecular enhancing methodology extended the conjugation length and red-shifted the molecule's absorption band to the excitation wavelength. It significantly enhanced the inherent cross sections of Raman scattering in the silent and fingerprint frequency regions for the characteristic vibrational modes of ν(C≡C), ν(O—N═O), $\nu(C_{Ph}—N)$, ν(C≡N), ν(C═C), and $\nu(C{\equiv}C_H)$, respectively.

Based on the AERS methodology, we obtained a library of AERS molecules including phenyl capped polyynes, nitrobenzene, azobenzene, benzonitrile, phenyl capped tetraene, and phenylacetylene. Extremely high sensitivity, e.g., ~10^4 level of RIE (relative Raman intensity versus EdU) and frequency

https://doi.org/10.1021/acscentsci.1c00117
ACS Cent. Sci. 2021, 7, 768−780

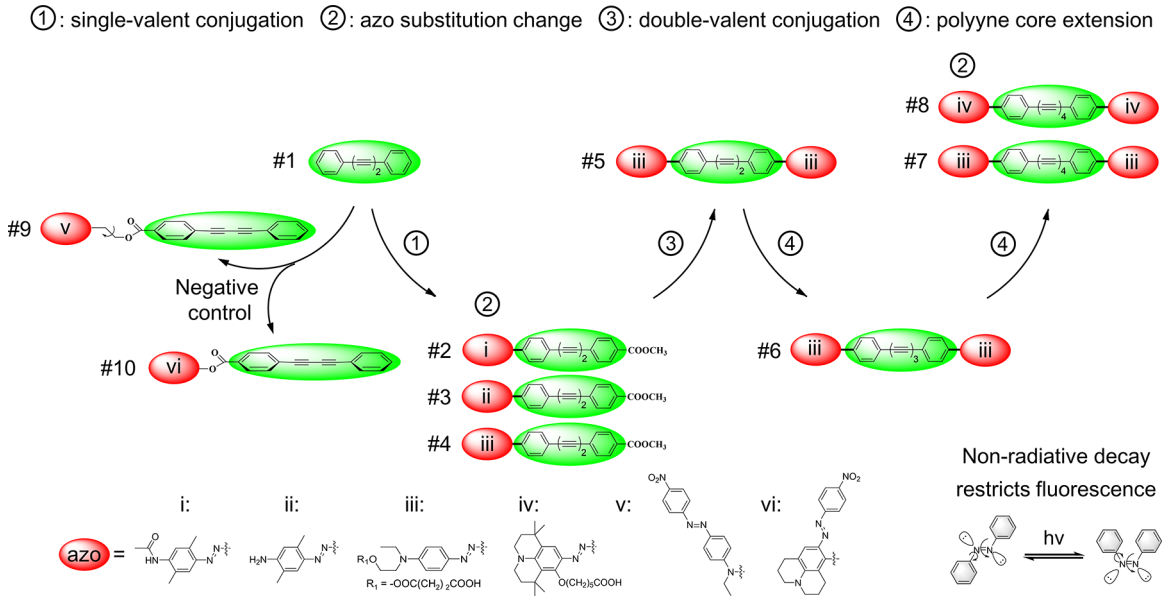

Figure 2. Enhancing strategies of azo-enhanced Raman scattering for phenyl capped polyynes. #1 represents the starting structure of vibrational mode ν(C≡C). #2−8 are the representative AERS polyynes. #9 and #10 are the representative diynes as the negative control without AERS effect.

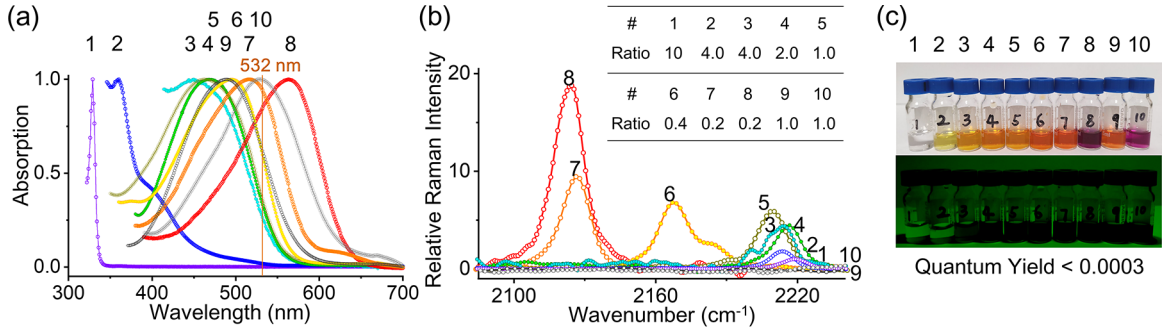

(d)

Molecule #	1	2	3	4	5	6	7	8	9	10
λ_{max} (nm)	329	360	450	467	463	494	516	563	489	527
ε at 532 nm (L·mol^{-1}·cm^{-1})	NA	408	1.21×10^4	1.14×10^4	9.5×10^3	3.26×10^4	3.58×10^4	3.89×10^4	2.79×10^4	2.16×10^4
Raman shift (cm^{-1})	2218	2214	2214	2216	2210	2167	2126	2125	2222	2220
RIE at 785 nm	16.7	45.8	94.8	49.6	105	232	753	491	36.4	8.4
RIE at 532 nm	24.1	106	278	525	1.42×10^3	5.96×10^3	1.22×10^4	3.10×10^4	Not seen	

Figure 3. Absorption, fluorescence, and Raman properties of the representative polyynes. (a) Absorption spectra. (b) Raman spectra at the frequency range of ν(C≡C). The Raman intensity of each molecule was normalized by that of Molecule #1 with the calculation of scaled concentration ratios. (c) Pictures of the compounds under room light and in the dark with 532 nm illumination. (d) Table of λ_{max}, molar extinction coefficients at 532 nm, Raman shift, and RIE at 785 and 532 nm excitation. RIE was calculated as the relative Raman intensities of each compound versus EdU.

tunability (10 frequency options) were achieved. We also demonstrated 6-color imaging of cellular organelles and 7-plex cell encoding applications using AERS probes and spontaneous Raman microscopy. This work will open new prospects to expand the applications of Raman spectroscopy and imaging for the ultrasensitive studies of trace amounts of entities in complicated systems.

RESULTS AND DISCUSSION

Structure Design of AERS Molecules. To achieve azo-enhanced Raman scattering, we explored the feasibility of conjugating azobenzene to phenyl capped polyynes and investigated the enhancing factors of ν(C≡C) bands in the silent frequency region. The schematic of enhancing strategies is presented in Figure 2. Azobenzene extended the $\pi-\pi$ conjugation system and allowed for red-shifting AERS

https://doi.org/10.1021/acscentsci.1c00117
ACS Cent. Sci. 2021, 7, 768−780

molecules' absorption into the visible region. Therefore, when being excited at the electronic resonance, the probability of vibrational transition was highly promoted due to the resonance Raman effect.

Typically, the process of resonance Raman scattering is accompanied by strong concomitant fluorescence that obscures the Raman spectrum. However, for the AERS molecules, the nonradiative decay of azobenzene from the excited state quenched the concomitant fluorescence, and thus provided a clean background for identifying the alkyne vibrational modes. The absorption, Raman scattering, and fluorescence of the representative polyynes were characterized and are shown in Figure 3. For additional comparison, we also measured the Raman spectra of commonly used resonant dyes and off-resonant Raman dyes. Their molecular structures and the raw spectra are shown Figure S2 (see the Supporting Information). The calculated RIE at different excitation wavelengths are also listed in Table S10 (see the Supporting Information).

Enhancing Mechanisms of AERS. For azo-enhanced Raman scattering, there are three types of factors that impact Raman sensitivity. The most important factor is the resonance Raman effect. The results in Figure 3a,d indicate that λ_{max} of Molecule #1−8 red-shifted from <300 nm to >500 nm. The molecules absorbed more light when the laser frequency (532 nm) overlapped with their absorption spectra. In this case, the electron resonance resulted in higher probability at the virtual state for the molecules, thus allowing for more intense Raman scattering. They produced increasing RIE, and eventually, the RIE was enhanced to a level of $\sim 10^4$ when the maximum absorption was located very close to 532 nm (e.g., Molecule #7 and #8, Figure 3b and d). The enhanced level of RIE was in good accordance with the distance between λ_{max} and 532 nm. For instance, both Molecule #2 and #3 had single-valent azobenzene conjugation. Their only difference was the substitution located at the azobenzene ring. The subsequent influence to the absorption λ_{max} was a 90 nm red shift for Molecule #3 compared to Molecule #2. As a result, Molecule #3 had more absorption at 532 nm excitation, which caused a higher level of resonance Raman scattering and an increased RIE of ∼2.6 times compared to Molecule #2.

The second factor is the extension of the π conjugation system. It was reported previously that the aromatic conjugation can enhance the Raman intensity of the alkyne stretching mode.[29] Similarly, the conjugation of azobenzene brings more atoms and electrons to the big π system, so the electrons are delocalized to a larger area, thus inducing more changes in the molecule's polarizability. For example, the azobenzene structure in Molecule #2 did not redshift the absorption to the desired level (far away from 532 nm excitation). However, a RIE enhancement of ∼4 times was still observed compared to Molecule #1. This was mainly due to the extension of π conjugation. The same finding was seen for Molecule #7 and #8 as well. They had approximately the same level of absorption at 532 nm. However, Molecule #8 had the ortho-alkxoyl substitution of julolidine, providing more electron density to the conjugation system. Therefore, the RIE of Molecule #8 increased by ∼2.5 times compared to Molecule #7 due to a larger conjugation system.

In order to compare the contribution of the resonance Raman effect and the conjugation effect, RIEs of the same compounds at 785 nm excitation were measured additionally. Because at 785 nm there was almost no absorption (Figure 3a and d), the Raman signals were measured off electron resonance in this case, and the enhancement was basically due to the conjugation effect. Based on the table shown in Figure 3d, with the stepwise increase of conjugation length from Molecule #1 → #4 → #5 → #6 → #7, the enhancement factor of Raman signals was 2−3 times for each of the steps. This signal enhancement was mainly due to the conjugation effect. Considering the enhancement caused by the resonance Raman effect, for Molecule #7 with the absorption close to 532 nm, its RIE at 532 nm excitation increased by a factor of 22 times compared with RIE at 785 nm excitation. This inferred that the resonance Raman effect was at a level of ∼10 times more significant than the conjugation effect. Therefore, the resonance Raman effect can be considered the dominant factor to influence the Raman enhancement.

In addition to the two major mechanisms of AERS, we explored the influence to Raman sensitivity resulting from the double-valent conjugation of azobenzenes at both terminals of the vibrational mode. Based on the comparison between Molecule #4 and #5, we found that the extension of a second azobenzene at the other terminal of polyyne further improved Raman intensity by ∼2.5 times. In this case, λ_{max} of Molecule #4 and #5 were approximately the same; therefore, their resonance Raman effect was considered at the same level and was not the main cause of the RIE enhancement. The observation of the RIE enhancement from Molecule #4 to #5 was due to the additional azobenzene extension that resulted in a higher level of symmetry, larger electron delocalization, and eventually bigger molecular polarizability for the molecule.

Besides the aforementioned enhancing mechanisms that can be realized by single-valent, double-valent conjugation of azobenzenes and azobenzene substitution change, the representative group of polyynes demonstrated an additional enhancing strategy of polyyne extension. From Molecule #5 to #6 and #6 to #7, the number of alkyne bonds increased from 2 to 3 and 3 to 4, respectively. The RIE was enhanced by ∼2.7 and ∼4.2 times, respectively. This enhancement level was lower than that of the resonance Raman effect (enhancement factor of ∼20). Although Molecule #5, #6, and #7 represented both azobenzene conjugation and polyyne extension, and the enhancing mechanisms included the electron-vibration resonance and the extension of π conjugation system, the Raman enhancement was mainly due to the resonance Raman effect resulting from azobenzene conjugation.

After systematically evaluating the positive influencing factors that cause RIE enhancement, we investigated a few molecular structures as negative controls to confirm the designing methodology. Molecule #9 and #10 were two diynes connected with azobenzene through ester bonds without coplanar conjugation. Although compared with Molecule #1 (the nonsubstituted diyne), λ_{max} increased from 329 to 489 and 527 nm due to the addition of azobenzene chromophore, the overlap of laser frequency with the absorption bands did not assist in enhancing RIE, compared with RIE at 785 nm excitation (off-resonant excitation, Figure 3d) for the mode of ν(C≡C). More interestingly, the Raman peaks of ν(C≡C) disappeared in the spectra. This is because the strong self-absorption of the azobenzene chromophore suppressed the Raman signals to a level that could not be detected. Therefore, in order to increase Raman intensities of the vibrational modes, the Resonance Raman effect caused by azobenzene conjugation has to be significant to surpass the concurrent strong

https://doi.org/10.1021/acscentsci.1c00117
ACS Cent. Sci. 2021, 7, 768−780

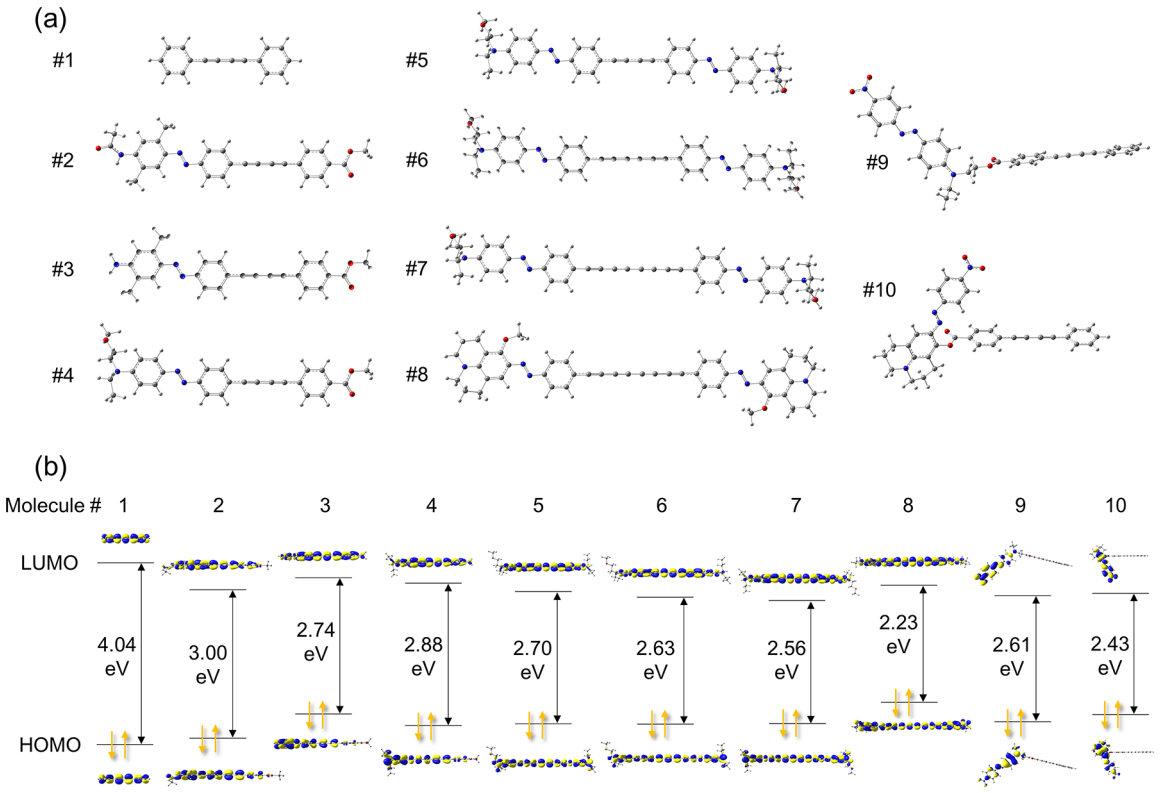

Figure 4. Results of DFT calculations. (a) Calculated molecular structures with the same skeletons of Molecule #1−10 in Figures 2 and 3. (b) Calculated highest occupied molecular orbitals (HOMO) and the lowest unoccupied molecular orbitals (LUMO) with the energy gaps.

absorption and maintain substantial signals of Raman scattering.

DFT Calculations of AERS Molecules. To better understand the photophysical properties of AERS molecules, the density functional theory (DFT) calculations were performed for the same molecular skeletons described above (see the calculation details in the Supporting Information). As shown in Figure 4a, the structures of Molecule #2−8 presented high degrees of coplanarity between polyynes and azobenzenes. In comparison, the coplanar extension was interrupted by the ester bond connection in Molecule #9 and #10. The angle between polyyne and azobenzene in Molecule #10 were 102.2°, while in Molecule #9, the connections included three σ bonds with free rotational flexibility.

The highest occupied molecular orbitals (HOMO) and the lowest unoccupied molecular orbitals (LUMO) are represented in Figure 4b. HOMO and LUMO electron density on the alkyne bonds were high in Molecule #2−8, further confirming a substantial π conjugation level between alkyne and azobenzene. The energy gaps from HOMO to LUMO were basically in agreement with the experimental data shown in Figure 3a and d.

Molecular Structure Flexibility of AERS. Following the designing methodology, we obtained a library of compounds to evaluate the enhancing factors of Raman intensities for eight different groups of vibrational modes including phenyl capped diynes, triynes, and tetraynes (Group A, B, and C), nitrobenzenes (Group D), azobenzenes (Group E), benzonitriles (Group F), phenyl capped tetraenes (Group G), and phenylacetylene (Group H). EdU was employed as a standard. The absolute Raman intensities of the compounds' specific peaks were compared to that of EdU's alkyne peak, in order to obtain RIE. Figure 5 presents the results in a matrix of RIE versus the Raman shift, and Table 1 summarizes the RIE data.

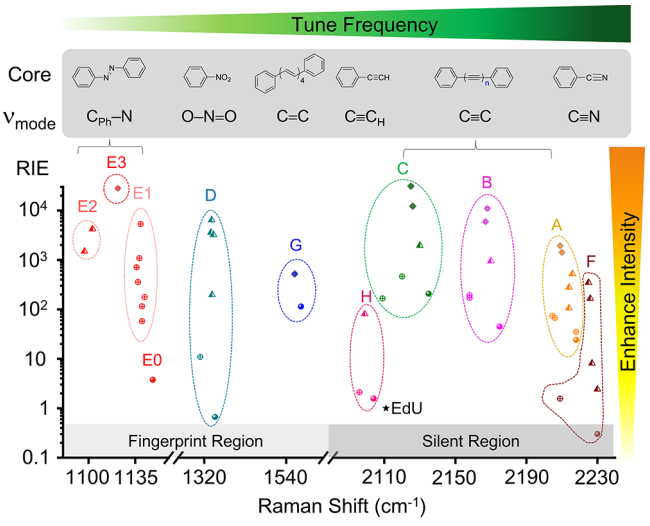

Figure 5. Azo-enhanced Raman properties of various vibrational modes, including Relative Raman Intensity versus EdU (RIE) and Raman shift. The corresponding vibrational modes are listed on the top of the figure.

The detailed structures and experimental data of all the synthesized compounds are provided in Tables S1−S8 of the Supporting Information.

It was observed that after azobenzene conjugation, Raman intensities of all groups (A−H) were significantly enhanced, while the fluorescence background was low when they were

https://doi.org/10.1021/acscentsci.1c00117
ACS Cent. Sci. 2021, 7, 768−780

Table 1. Average RIE and Range of Raman Shift for AERS Molecules[a]

Group	Structure	# of compounds	Raman Shift (cm^{-1})	Average RIE	Group	Structure	# of compounds	Raman Shift (cm^{-1})	Average RIE
A0	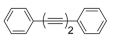	1	2218	24.1	B0	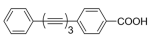	1	2175	44.8
A1	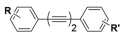	3	~2210	58.3	B1	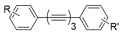	2	~2160	182
A2	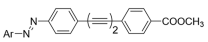	3	~2215	303	B2	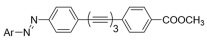	1	2170	952
A3	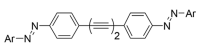	2	~2210	1.68×10^3	B3	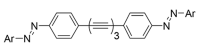	2	~2168	8.48×10^3
C0	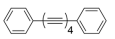	1	2135	207	D0		1	1349	0.67
C1	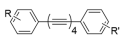	2	~2120	315	D1	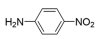	1	1309	10.9
C2	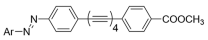	1	2130	1.95×10^3					
C3	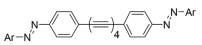	2	~2125	2.16×10^4	D2	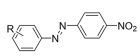	4	~1340	3.37×10^3
E0	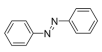	1	1148	3.77	F0		1	2230	0.31
E1	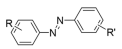	7	~1145	1.12×10^3	F1	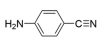	1	2209	1.56
E2	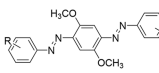	2	~1100	2.86×10^3					
E3	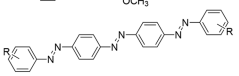	1	1120	2.81×10^4	F2	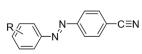	4	~2227	131
G0	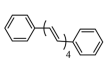	1	1580	114	H0		1	2104	1.24
					H1	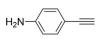	1	2096	2.10
G1	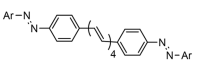	1	1563	521	H2	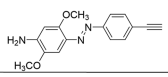	1	2099	80.6

[a]The compounds are divided into eight major groups of A, B, C, D, E, F, G, and H based on the molecular structures. Each major group includes subgroups consisting of a single or multiple compounds.

excited at 532 nm. There were approximately 2 orders of magnitude for the maximum RIE enhancing factors of alkyne AERS compounds compared to their corresponding basic vibrational modes A0, B0, and C0. Specifically, RIE of azobenzene-capped tetrayne with julolidine moieties increased to $>10^4$ level among all the alkyne compounds, because tetrayne has the basic Raman intensity superior to that of diyne and triyne. For nitro compounds, although the intensity of nitrobenzene was not intense, nitrobenzene with a julolidine moiety after azobenzene conjugation presented the highest enhancing factor among all groups of compounds, which was ~5000 times intensity increase compared to D0 for the mode of ν(O—N═O). For nitrile compounds, there was approximately ~400 times intensity enhancement for the mode of ν(C≡N) at 2225 cm^{-1} in the silent region, but their absolute intensity level was not competitive compared to $\nu(C_{Ph}—N)$ of the same molecule (Table S6 of the Supporting Information); therefore, the latter one may have more potential for Raman imaging applications.

Besides enhancing the intrinsic Raman intensities for AERS molecules, the methodology provides an important solution to tune Raman frequencies based on the specific vibrational modes. Considering the phenyl-capped polyynes, their Raman shift moved from 2210 to 2170 and further to 2125 cm^{-1} when the number of conjugated alkynes increased from 2 to 3 and 4, respectively. As these peaks were uniquely located at the silent region without interference from other signals, considering the enhanced sensitivity (maximum RIE of ~10^4 level) and the natural separation between the Raman shifts, AERS phenyl-capped polyynes are ideal candidates for applications of multicolor detection or imaging.

Azobenzene-based AERS molecules are another important group. Through the additional conjugation of a second azobenzene to 2,5-dimethoxyazobenzene, the frequency of $\nu(C_{Ph}—N)$ shifted from ~1145 cm^{-1} (Group E1) to ~1100 cm^{-1} (Group E2). When two azobenzenes were conjugated at both terminals, the frequency shifted to ~1120 cm^{-1} (Group E3). These characteristic peaks of $\nu(C_{Ph}—N)$ were located at the fingerprint region where signal interference typically exists.

https://doi.org/10.1021/acscentsci.1c00117
ACS Cent. Sci. 2021, 7, 768−780

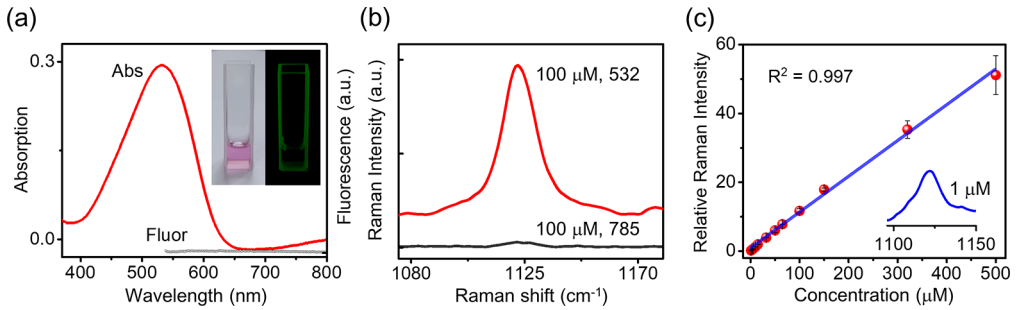

Figure 6. Spectral properties of Azo-3. (a) Absorption and fluorescence spectra of 5.0 μM of Azo-3. (b) Raman signal of $\nu(C_{Ph}—N)$ for 100 μM of Azo-3 excited by 532 and 785 nm laser. (c) Linear relationship between the relative Raman intensity and the Azo-3 concentration. The relative Raman intensity was obtained by normalizing the Raman peak of Azo-3 to that of the solvent peak at ~867 cm^{-1}. The inset shows the signal level of 1.0 μM of Azo-3.

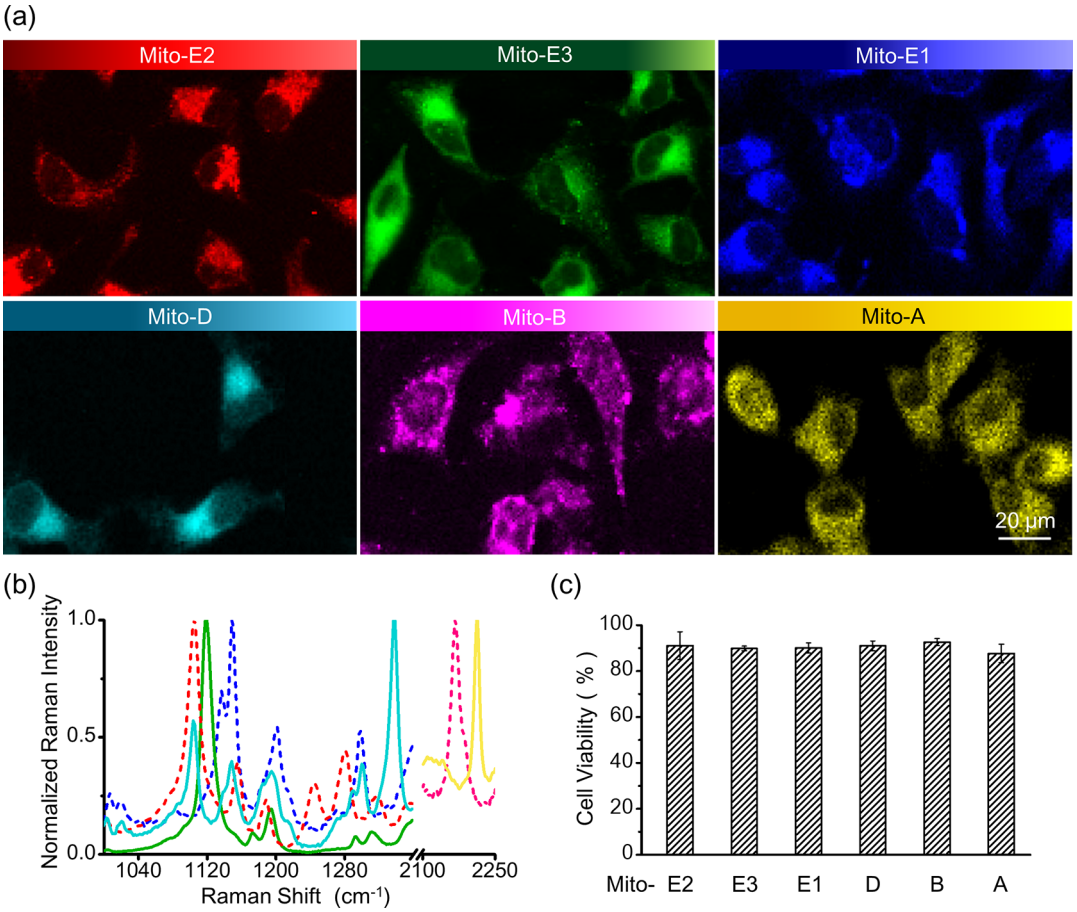

Figure 7. Multicolor AERS images of live cells. (a) Raman images of HeLa cells stained with each probe shown in the respective pseudo color. (b) Averaged Raman spectra of HeLa cells stained by each probe are shown as the lines in the corresponding colors. Raman spectra were self-normalized by the characteristic peaks in the Raman shift regions of interest. (c) Toxicity of the six AERS probes.

However, the enhanced peak intensity/sensitivity (maximum RIE of ~10^4 level) minimized the interference, and the frequency separation ≥15 cm^{-1} provides a foundation for selecting multicolor frequencies from this group of compounds.

In addition, nitrobenzene based AERS molecules have exceptional RIE as well (maximum RIE of ~10^3 level). They presented well-separated and distinct frequencies of ν(O—N═O) in the fingerprint region, thus allowing for potential multicolor applications. Besides these three major groups, the remaining groups of compounds with the structures of phenyl-capped tetraenes, benzonitriles, and phenyl acetylenes provide other multicolor options, due to their specific frequencies of ν(C═C), ν(C≡N), and $\nu(C{\equiv}C_H)$ in the fingerprint region and silent region, respectively. However, their relatively low Raman intensities may hinder their applications.

Based on the discussion above, one has to evaluate the selection of the peak intensities and Raman shifts, when compounds from various groups of AERS molecules are combined for multicolor detection/imaging. Noticeably, each AERS molecule contains azobenzene as an enhancing unit and may present a similar peak at similar frequency. Therefore, if a compound from Group E1 is selected, one may have to utilize more complex hyperspectral analysis methods to decode

https://doi.org/10.1021/acscentsci.1c00117
ACS Cent. Sci. 2021, 7, 768−780

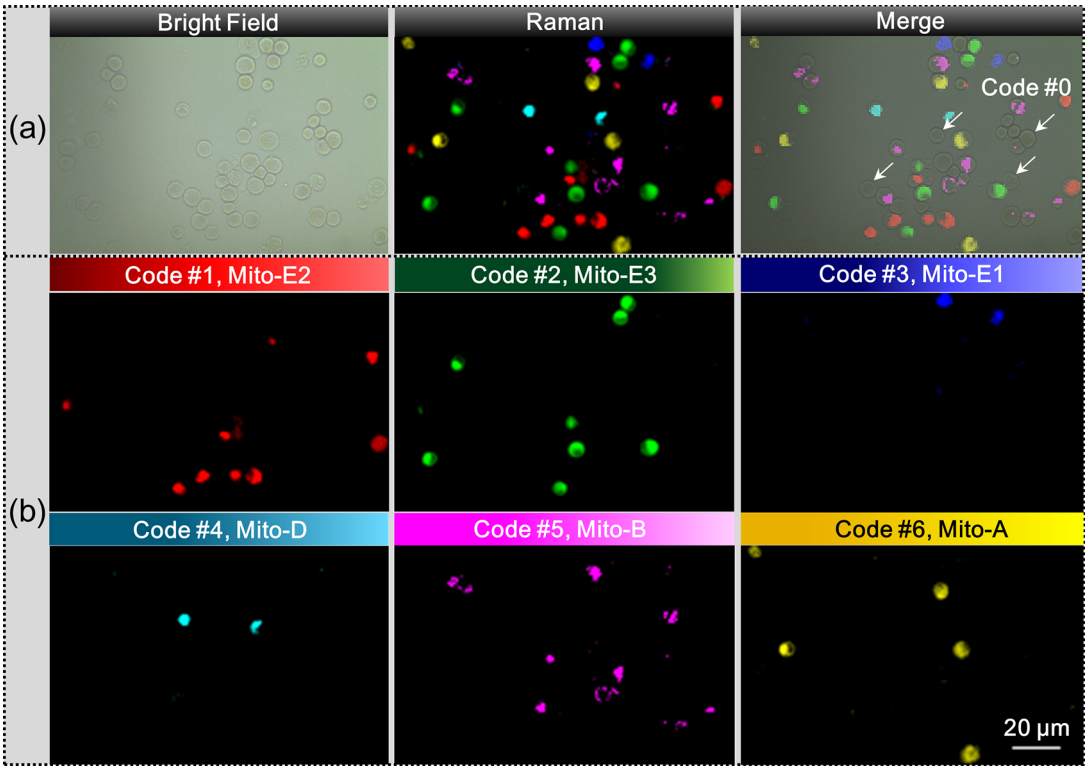

Figure 8. Multiplex AERS coded images of mixed suspended HeLa cells. (a) Bright-field, Raman, and their overlay images of HeLa cells. Cells with the same extracted Raman spectra were presented in the same pseudo color, while the information on Raman intensity at each pixel was fully maintained. (b) Extracted Raman images of the six codes of cells based on six different types of Raman spectra shown in Figure 7b, representing Code #1 (Mito-E2), #2 (Mito-E3), #3 (Mito-E1), #4 (Mito-D), #5 (Mito-B), and #6 (Mito-A), respectively.

compounds from other groups and differentiate them from Group E1 based on their additional characteristic vibrational frequencies other than $\nu(C_{Ph}—N)$ of Group E1.

Spectral Properties of Ultrasensitive Azo-3. Azo-3 was one of the most intense AERS molecules among all eight groups and have high solubility in water. It was synthesized as the only representative compound in Group E3 (E3.1). We explored the spectral characteristics of Azo-3 to clarify its absorption, Raman, and fluorescence properties. As shown in Figure 6a, Azo-3 had maximum absorption close to 532 nm, matching the laser wavelength of typical commercial Raman microscopes. It produced substantially low fluorescence background when illuminated at 532 nm. The comparison of Raman spectra of 100 μM Azo-3 at 532 and 785 nm excitation evidenced that the Raman intensity of $\nu(C_{Ph}—N)$ at 1120 cm^{-1} significantly increased at electron resonance, while only a small peak was seen at 785 nm excitation without the resonance Raman effect (Figure 6b).

When we measured the Raman intensities of Azo-3 at different concentrations (Figure 6c), the calibration curve resulted in a linear relationship between the signals and concentrations in the range of 1.0−500 μM. Higher concentrations of Azo-3 induced a greater amount of light absorption which caused a decrease of the Raman intensity. This linear range of more than 2 orders of magnitude is considered efficient for potential applications of quantifying molecules of interest if Azo-3 is used as the signal reporter.

Demonstration of Multicolor AERS Imaging. In order to demonstrate an application of multicolor AERS imaging, we synthesized two AERS probes, Mito-E3 with a triphenylphosphonium cation (TPP^+) and Lyso-D with an *N*,*N*-dimethylethylenediamine moiety to target cellular organelles mitochondria and lysosomes, respectively. HeLa cells were incubated with the probes and the fluorescent dyes simultaneously to stain the same organelles and confirm their colocolization, e.g., Mito-E3/MitoTrackerRed and Lyso-D/LysoTrackerRed, respectively. The results evidenced that Raman and fluorescent dyes were located consistently within the same cell (Figure S3 in the Supporting Information). In addition, the photostability of Mito-E3 and MitoTrackerRed were tested after multiple imaging scans. It confirmed that the AERS probe still maintained photostable imaging after 15 scans under a 532 nm laser of 0.5 mw power, while the fluorescence of the fluorescent probe quenched dramatically after a couple of scans (Figure S4 in the Supporting Information).

To expand the frequency options for imaging live cells with multicolor, we synthesized Mito-E2, Mito-E1, Mito-D, Mito-B, and Mito-A besides Mito-E3, by functionalizing each reporter with TPP^+ at the terminals (see the detailed molecular structures in the Supporting Information). After HeLa cells were incubated with these AERS probes separately, they were imaged by a confocal Raman microscope at 532 nm. Figure 7a shows the respective Raman images of live HeLa cells stained with the six probes. The specific Raman peaks identified from the averaged spectra of cells were located at 1105, 1118, 1148, 1337, 2167, and 2213 cm^{-1}, respectively (Figure 7b). After being tested by Invitrogen Live/Dead Viability/Cytotoxicity kit, the toxicity of all probes was found to be low (Figure 7c).

The imaging results evidence that Mito-E3 produced an image with the highest quality. This is mainly due to its high Raman sensitivity (Figure 5). Mito-E2 and Mito-E1 produced high-quality images as well, although their Raman sensitivities

https://doi.org/10.1021/acscentsci.1c00117
ACS Cent. Sci. 2021, 7, 768−780

were slightly lower. The images of HeLa cells stained with Mito-D, Mito-B, and Mito-A were recognizable, although the imaging quality was not superior to Mito-E2, Mito-E3, and Mito-E1. We also synthesized Mito-C based on its parent AERS compound C3.1, since C3.1 had a very strong Raman peak at 2126 cm^{-1} (RIE 1.22 × 10^4, Figure 5, Table 1, and Table S3). Interestingly, the mitochondria probe Mito-C with a triphenylphosphonium cation (TPP^+) moiety failed to produce a recognizable Raman image after being incubated with cells at 5−10 μM. It is possibly due to the tetrayne structure which might result in poor trans-membrane ability. Therefore, for multicolor Raman imaging of live cells using an AERS probe, the imaging quality is critically related to the intrinsic sensitivity of the probe and other influencing factors including the probe's solubility in cell culture (see the details in the Experimental Section), the penetration efficiency when entering cells and the subsequent staining efficiency when targeting specific organelles. After briefly investigating these factors during the probe design/synthesis and cell staining/imaging processes, we found Mito-E2, Mito-E3, Mito-E1, Mito-D, Mito-B, and Mito-A were highly applicable AERS probes for multicolor Raman imaging of live cells (Figure 7).

Demonstration of Multiplex AERS Coding. When different types of entities have interactions in a mixture, it will be useful to encode/identify individual entities and track the reactions. As an example, fluorescent probes have been popularly used to encode cells in a mixture to track intercellular reactions. However, when the involved mixture of different cells become complicated, it is challenging to detect a larger number of signal channels due to the broad and overlapping fluorescence bands.[51−55] The power of AERS was investigated to encode/decode cells in a mixture by applying multiple AERS probes.

Experimentally, when the adherent HeLa Cells were stained with various mitochondria probes (Mito-E2, Mito-E3, Mito-E1, Mito-D, Mito-B, and Mito-A), the cells were labeled with different Raman codes presenting scattering signals at different Raman shifts. We digested, resuspended, and mixed these cells in PBS buffer. Unstained suspended cells were also added into this mixture as Code #0. Then, each cell in the mixture was encoded by a specific Raman spectrum resulting from its exogenous AERS probe or from itself. Eventually the mixed sample included all seven different types of cells with preassigned Code #0−6. We measured this sample for the bright-field and Raman images under a confocal Raman microscope (Figure 8a).

Although the bright-field image could not provide any information for the cell codes due to the lack of spectral information, the Raman image contained the complete spectral information at each pixel in the image. Therefore, we were able to identify each Raman-coded cell from the mixture by extracting the averaged spectrum of the cell and comparing it with the standard spectrum of each AERS probe shown in Figure 7b (see the details in the Supporting Information). Figure 8b presents the seven clearly identified codes of cells (Code #0−6) based on this method. The result indicates that a new research area of exploring more AERS probes for live-cell imaging/encoding can be developed by selecting the structures of vibrational modes, azo-enhanced strategies, and targeting groups. The efficacy of cellular AERS probes can be optimized based on multiple factors including the signal sensitivity, solubility, targeting specificity, and penetration/staining efficiency of the probes, etc.

CONCLUSION

In order to take advantage of the narrow bandwidths of Raman spectra and overcome the major obstacle of low Raman sensitivity of molecular vibrations, we reported a new concept of azo-enhanced Raman scattering. By conjugating azobenzenes to various vibrational modes, the intensity of the vibrational modes was enhanced while the concomitant fluorescence was suppressed significantly. The structures of vibrational modes include phenyl capped polyynes, nitrobenzene, azobenzene, benzonitrile, phenyl capped tetraene, and phenylacetylene. Their corresponding vibrational modes are $\nu(C{\equiv}C)$, $\nu(O{-}N{=}O)$, $\nu(C_{Ph}{-}N)$, $\nu(C{\equiv}N)$, $\nu(C{=}C)$, and $\nu(C{\equiv}C_H)$ in the silent and fingerprint regions of Raman shift. Based on the methodology, we obtained a library of AERS molecules. The synthesized AERS molecules produced RIE of more than 4 orders of magnitude and frequency tunability of 10 distinct spectral bands.

The experimental and simulation results indicate that the occurrence of AERS was related to the electron-vibration resonance, the extension of conjugation system, and the symmetric level of the vibrational mode. These fundamental enhancing mechanisms can be realized using various strategies to design molecular structures, including single-valent conjugation of azobenzene, azobenzene substitution change, double-valent conjugation of azobenzenes, and extension of the structure of vibrational modes.

Using the enhancing mechanisms of AERS, we synthesized ultrasensitive AERS probes to target cellular organelles. The application of multiple mitochondria AERS probes was demonstrated for multicolor imaging of live cells using spontaneous Raman microscopy. The investigation of the probe design/synthesis and cell staining/imaging process identified highly applicable AERS probes Mito-E2, Mito-E3, Mito-E1, Mito-D, Mito-B, and Mito-A at distinct fingerprint and silent frequency regions. A further study of encoding different cells in a mixture with 7 multiplicity confirmed the feasibility and accuracy of AERS labeling/probing method. These applications imply the great potential of utilizing AERS probes to track cellular organelles and/or intracellular/intercellular reactions. The work will inspire new prospects to explore innovative applications of AERS for ultrasensitive studies of other trace entities within complicated systems in multidisciplinary research fields.

EXPERIMENTAL SECTION

Materials. All synthetic reagents and solvents were purchased from Shanghai Aladdin Bio-Chem, Sinopharm Chemical Reagent, and Bidepharm Co. HeLa cells were obtained from China Center for Type Culture Collection (Wuhan, China) and cultured in DMEM (Invitrogen) supplemented with 10% FBS (Invitrogen) and 1% antibiotics (penicillin/streptomycin, Invitrogen). All cells were maintained in a humidified 5% CO_2 incubator at 37 °C. MitoTracker Red CMXRos and LysoTracker Red DND-99 were purchased from Dalian Meilun Biotechnology Co. Live/Dead Viability/Cytotoxicity kit was obtained from Invitrogen.

Confocal Raman Spectroscopy. Raman spectra were obtained using a Renishaw inVia reflex spectrometer, operating with 532 nm laser and a thermoelectrically cooled CCD, coupled to a Leica DM LM microscope (50× air objective, NA 0.75). The spectral resolution is 2 cm^{-1}. The calibration of the wavenumber axis was done by recording the Raman spectrum

https://doi.org/10.1021/acscentsci.1c00117
ACS Cent. Sci. 2021, 7, 768−780

of the silicon wafer (1 accumulation, 10 s) in the static mode. The laser power was 5 mW. When each sample was measured, 5 or 10 frames were collected to average the signals and background noise, where each spectra frame was measured for 2 s exposure. Some of the raw spectra were processed by automatic smoothing/baseline correction when needed.

Each AERS compound was dissolved in *N*,*N*-dimethylformamide (DMF) at a concentration dependent on the Raman intensity of the compound. 4 μL of the solution was placed on a silicon wafer for Raman spectra measurements. The characteristic peaks were automatically fitted with a Gaussian function for peak areas by Matlab. The RIE (relative Raman intensity vs EdU) was calculated as the peak area ratio of the AERS compound vs that of EdU. While EdU and each AERS compound were prepared individually in DMF at very dilute concentrations (typically 0.01−100 mM), the peak of DMF at 867 cm^{-1} was used as the reference of internal standard to conduct the calculations. The peak area ratio of the compound versus DMF was maintained in a range of 0.1−10; otherwise, the compound concentration was changed accordingly. In case the characteristic peaks of some AERS compounds overlapped with that of DMF, *N*-methylpyrrolidone (NMP) was used as the alternative solvent and internal standard. The peak of NMP at 927 cm^{-1} was then used to calculate RIE.

UV−vis Absorption Spectroscopy. 1 mL of each AERS compound solution in DMF was placed in a cuvette and measured by an Agilent Cary 60 UV−vis spectrometer, at an appropriate concentration in the range of 0.01−1 mM dependent on the absorption level of the compound. In cases the absorption of some AERS compounds overlapped with that of DMF at wavelength <300 nm, methanol or acetonitrile was used as the alternative solvent. The values of λ_{max} were determined by reading the first absorption peak that could be identified clearly starting from the longer wavelength.

Colocalization Experiment. HeLa cells were cultured in clean quartz Petri dishes for 24 h. Mitochondria staining was done by incubating HeLa cells in the growth medium at 37 °C for 1 h with 5 μM of Mito-E3 and 0.2 μM of MitoTracker Red CMXRos together. Lysosome staining was done using the same procedure with 5 μM of Lyso-D and 0.2 μM of LysoTracker Red DND-99. Raman images were obtained using a Renishaw inVia reflex microscope (63× water objective, NA 1.20) and 5 mW of 532 nm laser. The scanning step was 1 μm and the scanning time for each pixel was 30 ms. The total imaging time was ∼2 min for an area of ∼70 μm × 50 μm. The laser power of 0.025 mW and 0.5 mW were used for imaging mitochondria and lysosome, respectively. For mitochondria imaging, the Raman signal was selected at the peak of 1118 cm^{-1} and the fluorescence signal was selected at 600 nm. For lysosome imaging, the Raman signal was selected at the peak of 1337 cm^{-1} and the fluorescence signal was selected in the range of 592 nm.

Multicolor Raman Imaging of Live HeLa Cells. HeLa cells were cultured in six clean quartz Petri dishes and then stained in culture medium at 37 °C for 2 h with 8 μM of Mito-A, Mito-B, and 5 μM of Mito-D, Mito-E1, Mito-E2, and Mito-E3. The Raman images were obtained using 532 nm laser at 5 mw, 63× water objective, and 1 μm scanning step. The scanning time for each pixel is 30 ms, and the total imaging time was ∼8 min for an area of ∼140 μm × 90 μm.

In cell staining and imaging experiments, the first step was to make a stock solution of the probe in DMSO. Most AERS compounds were soluble at 10^{-3} M in DMSO except C3.1 and C3.2 with lower solubility. C3.1 was soluble at 3×10^{-4} M and C3.2 was soluble at 2×10^{-5} M in DMSO. It was found that the probes' solubility was higher than their parent AERS compounds in both DMSO and PBS, due to the addition of the targeting groups, e.g., triphenylphosphonium cation (TPP^+) for targeting mitochondria and the *N*,*N*-dimethylethylenediamine moiety for targeting lysosomes. We found all of the probes were soluble at 10^{-2} M in DMSO. Then, for targeting organelles and targeting live cells, the stock solutions (Mito-A, Mito-B, Mito-D, Mito-E1, Mito-E2, Mito-E3, and Lyso-D) were made at 10^{-3} M in DMSO and diluted to the desired concentration in PBS before it was added into cell culture for staining. Mito-B, Mito-D, Mito-E1, Mito E3, and Lyso-D were soluble at 100 μM in PBS, and Mito-A and Mito-E2 were soluble at 20 μM in PBS. In order to minimize the possible toxicity of the probes to cells while maintaining good imaging quality, their eventual staining concentrations were kept in the range of 5−10 μM.

Multicolor Imaging of Raman Codes of Mixed HeLa Cells. HeLa cells were trypsinized with 0.05% trypsin-EDTA from the bottom of a T75 flask, neutralized with DMEM, and then divided equally into seven clean quartz Petri dishes. Cells in each of the first six dishes were stained with one of the mitochondria AERS probes at the concentration of 8 μM in culture medium at 37 °C for 2 h, including Mito-A, Mito-B, Mito-D, Mito-E1, Mito-E2, and Mito-E3, respectively. Then, all of them were mixed together with the untreated cells in the seventh dish, and then centrifuged at 1000 rpm for 2 min. The cells were washed with PBS and then centrifuged again at 1000 rpm for 2 min. This step was repeated 2 times. Then, 10 μL of suspended cells were placed on a quartz slide under the confocal Raman microscope (20× air objective, NA 0.40) for imaging. The Raman image was obtained using 532 nm laser at 5 mw and 3 μm scanning step. The scanning time for each pixel is 30 ms, and the total imaging time was ∼9 min for an area of ∼400 μm × 300 μm.

To generate the false-colored Raman images, the original hyperspectral datacube was first background-subtracted using Asymmetric Least Squares,[56] and then, the spectral regions where the compounds had strong peaks was averaged to generate an image from which individual cells could be identified. A simple watershed segmentation algorithm separated the image into individual cells,[57] whose signals were averaged together to generate "cell-level" spectra. These cell-level spectra were then cropped to the region from 1050 to 1350 relative wavenumbers and 2100 to 2250 relative wavenumbers, which captured all of the major peaks of the spectral labels. These cropped spectra were then vector-normalized, and the blind unmixing algorithm Vertex Component Analysis (VCA)[58] was used to automatically identify the spectra of the individual labels. The outputs of VCA were "guesses" of the pure components of the data set (in this case the individual labeled spectra), where the guesses were referred to as "endmembers". Once the endmembers were identified, the original unnormalized data set was fit pixel by pixel using the endmember spectra through non-negative least-squares.

Cell Viability Assays. In order to test the cytotoxicity of each AERS probe, HeLa cells were separately seeded on three clean quartz Petri dishes. For one of the Petri dishes, cells were incubated with each of the AERS probes at 5 μM concentration in culture medium for 2 h. The AERS probes were Mito-A, Mito-B, Mito-D, Mito-E1, Mito-E2, and Mito-

https://doi.org/10.1021/acscentsci.1c00117
ACS Cent. Sci. 2021, 7, 768−780

E3. The other two Petri dishes were used as positive (live cells) and negative (dead cells) controls, representing nontreated cells in culture medium and cells fixed with the same amount of medium including 70% alcohol for 30 min. After the treatment was done, the culture medium was removed, and the cells were washed with PBS for 3 times. In order to test the relationship between the cytotoxicity of Mito-E3 and the staining time, the same procedure was followed as described above except changing the staining time in the range of 0.5−4 h.

Cell viability assays were performed using Invitrogen Live/Dead Viability/Cytotoxicity kit. The staining concentrations of the reagents in the kit were 2 μM for Calcein AM and 4 μM for EthD-1. The staining time was 30 min at 37 °C. After staining, cells were placed under the confocal fluorescence microscope (Leica TCS SP8) for imaging. The excitation/emission wavelengths for Calcein AM and EthD-1 were 488/530 and 514/645, respectively.

■ ASSOCIATED CONTENT

Supporting Information

The Supporting Information is available free of charge at https://pubs.acs.org/doi/10.1021/acscentsci.1c00117.

Supplementary spectral data, DFT calculations, imaging data and analysis, synthesis and characterization of AERS compounds (PDF)

■ AUTHOR INFORMATION

Corresponding Authors

Yuchen Tang − *China Key Laboratory of Pesticide and Chemical Biology of Ministry of Education, Wuhan 430079, China; College of Chemistry, Central China Normal University, Wuhan 430079, China*; Email: ytang@mail.ccnu.edu.cn

Tingjuan Gao − *China Key Laboratory of Pesticide and Chemical Biology of Ministry of Education, Wuhan 430079, China; College of Chemistry, Central China Normal University, Wuhan 430079, China*; orcid.org/0000-0002-1586-9265; Email: tingao@mail.ccnu.edu.cn

Authors

Yongpeng Zhuang − *China Key Laboratory of Pesticide and Chemical Biology of Ministry of Education, Wuhan 430079, China; College of Chemistry, Central China Normal University, Wuhan 430079, China*

Shaohua Zhang − *China Key Laboratory of Pesticide and Chemical Biology of Ministry of Education, Wuhan 430079, China; College of Chemistry, Central China Normal University, Wuhan 430079, China*

Zachary J. Smith − *Department of Precision Machinery and Precision Instrumentation, University of Science and Technology of China, Hefei 230027, China*; orcid.org/0000-0002-7946-7863

Yuee Li − *School of Information Science and Engineering, Lanzhou University, Lanzhou 730000, China*; orcid.org/0000-0001-5430-1587

Xijiao Mu − *School of Information Science and Engineering, Lanzhou University, Lanzhou 730000, China*; orcid.org/0000-0002-7991-0669

Mengna Li − *China Key Laboratory of Pesticide and Chemical Biology of Ministry of Education, Wuhan 430079, China; College of Chemistry, Central China Normal University, Wuhan 430079, China*

Caili He − *China Key Laboratory of Pesticide and Chemical Biology of Ministry of Education, Wuhan 430079, China; College of Chemistry, Central China Normal University, Wuhan 430079, China*

Xingxing Zheng − *China Key Laboratory of Pesticide and Chemical Biology of Ministry of Education, Wuhan 430079, China; College of Chemistry, Central China Normal University, Wuhan 430079, China*

Fangfang Pan − *China Key Laboratory of Pesticide and Chemical Biology of Ministry of Education, Wuhan 430079, China; College of Chemistry, Central China Normal University, Wuhan 430079, China*; orcid.org/0000-0002-3091-6795

Lizhi Zhang − *China Key Laboratory of Pesticide and Chemical Biology of Ministry of Education, Wuhan 430079, China; College of Chemistry, Central China Normal University, Wuhan 430079, China*; orcid.org/0000-0002-6842-9167

Complete contact information is available at: https://pubs.acs.org/10.1021/acscentsci.1c00117

Notes

The authors declare no competing financial interest.

■ ACKNOWLEDGMENTS

This work is supported by the National Natural Science Foundation of China (21605054, 22076058), Central China Normal University (CCNU) new PI start-up fund (210-31102). T.G. acknowledges support from the Program of Introducing Talents of Discipline to University of China (111 program, B17019). L.Z. acknowledges support from the National Key Research and Development Program of China (2018YFC1800701).

■ REFERENCES

(1) Freudiger, C. W.; Min, W.; Saar, B. G.; Lu, S.; Holtom, G. R.; He, C.; Tsai, J. C.; Kang, J. X.; Xie, X. S. Label-free biomedical imaging with high sensitivity by stimulated Raman scattering microscopy. *Science* **2008**, *322*, 1857−1861.

(2) Fu, D.; Lu, F.-K.; Zhang, X.; Freudiger, C.; Pernik, D. R.; Holtom, G.; Xie, X. S. Quantitative chemical imaging with multiplex stimulated Raman scattering microscopy. *J. Am. Chem. Soc.* **2012**, *134*, 3623−3626.

(3) Wei, L.; Yu, Y.; Shen, Y.; Wang, M. C.; Min, W. Vibrational imaging of newly synthesized proteins in live cells by stimulated Raman scattering microscopy. *Proc. Natl. Acad. Sci. U. S. A.* **2013**, *110*, 11226−11231.

(4) Wei, L.; Chen, Z.; Shi, L.; Long, R.; Anzalone, A. V.; Zhang, L.; Hu, F.; Yuste, R.; Cornish, V. W.; Min, W. Super-multiplex vibrational imaging. *Nature* **2017**, *544*, 465−470.

(5) Hu, F.; Zeng, C.; Long, R.; Miao, Y.; Wei, L.; Xu, Q.; Min, W. Supermultiplexed optical imaging and barcoding with engineered polyynes. *Nat. Methods* **2018**, *15*, 194.

(6) Tang, Y.; He, C.; Zheng, X.; Chen, X.; Gao, T. Super-capacity information-carrying systems encoded with spontaneous Raman scattering. *Chem. Sci.* **2020**, *11*, 3096−3103.

(7) Puppels, G. J.; de Mul, F. F. M.; Otto, C.; Greve, J.; Robert-Nicoud, M.; Arndt-Jovin, D. J.; Jovin, T. M. Studying single living cells and chromosomes by confocal Raman microspectroscopy. *Nature* **1990**, *347*, 301−303.

(8) Keren, S.; Zavaleta, C.; Cheng, Z.; de la Zerda, A.; Gheysens, O.; Gambhir, S. S. Noninvasive molecular imaging of small living subjects

using Raman spectroscopy. *Proc. Natl. Acad. Sci. U. S. A.* **2008**, *105*, 5844−5849.
(9) Abramczyk, H.; Brozek-Pluska, B. Raman imaging in biochemical and biomedical applications. Diagnosis and treatment of breast cancer. *Chem. Rev.* **2013**, *113*, 5766−5781.
(10) Pence, I.; Mahadevan-Jansen, A. Clinical instrumentation and applications of Raman spectroscopy. *Chem. Soc. Rev.* **2016**, *45*, 1958−1979.
(11) Smith, R.; Wright, K. L.; Ashton, L. Raman spectroscopy: an evolving technique for live cell studies. *Analyst* **2016**, *141*, 3590−3600.
(12) Zumbusch, A.; Holtom, G. R.; Xie, X. S. Three-dimensional vibrational imaging by coherent anti-Stokes Raman scattering. *Phys. Rev. Lett.* **1999**, *82*, 4142.
(13) Xie, X. S.; Yu, J.; Yang, W. Y. Living cells as test tubes. *Science* **2006**, *312*, 228−230.
(14) Saar, B. G.; Freudiger, C. W.; Reichman, J.; Stanley, C. M.; Holtom, G. R.; Xie, X. S. Video-rate molecular imaging in vivo with stimulated Raman scattering. *Science* **2010**, *330*, 1368−1370.
(15) Arzumanyan, G. M.; Doroshkevich, N. V.; Mamatkulov, K. Z.; Shashkov, S. N.; Zinovev, E. V.; Vlasov, A. V.; Round, E. S.; Gordeliy, V. I. Highly sensitive coherent anti-stokes Raman scattering imaging of protein crystals. *J. Am. Chem. Soc.* **2016**, *138*, 13457−13460.
(16) Krafft, C.; Schie, I. W.; Meyer, T.; Schmitt, M.; Popp, J. Developments in spontaneous and coherent Raman scattering microscopic imaging for biomedical applications. *Chem. Soc. Rev.* **2016**, *45*, 1819−1849.
(17) Wei, L.; Hu, F.; Chen, Z.; Shen, Y.; Zhang, L.; Min, W. Live-cell bioorthogonal chemical imaging: stimulated Raman scattering microscopy of vibrational probes. *Acc. Chem. Res.* **2016**, *49*, 1494−1502.
(18) Fu, D.; Yang, W.; Xie, X. S. Label-free imaging of neurotransmitter acetylcholine at neuromuscular junctions with stimulated Raman scattering. *J. Am. Chem. Soc.* **2017**, *139*, 583−586.
(19) Zhao, Z.; Chen, C.; Wei, S.; Xiong, H.; Hu, F.; Miao, Y.; Jin, T.; Min, W. Ultra-bright Raman dots for multiplexed optical imaging. *Nat. Commun.* **2021**, *12*, 1305.
(20) Qian, X. M.; Nie, S. M. Single-molecule and single-nanoparticle SERS: from fundamental mechanisms to biomedical applications. *Chem. Soc. Rev.* **2008**, *37*, 912−920.
(21) Kneipp, J.; Kneipp, H.; Kneipp, K. SERS - a single-molecule and nanoscale tool for bioanalytics. *Chem. Soc. Rev.* **2008**, *37*, 1052−1060.
(22) Hu, Q.; Tay, L.-L.; Noestheden, M.; Pezacki, J. P. Mammalian cell surface imaging with nitrile-functionalized nanoprobes: biophysical characterization of aggregation and polarization anisotropy in SERS imaging. *J. Am. Chem. Soc.* **2007**, *129*, 14−15.
(23) Nam, J. M.; Oh, J. W.; Lee, H.; Suh, Y. D. Plasmonic nanogap-enhanced Raman scattering with nanoparticles. *Acc. Chem. Res.* **2016**, *49*, 2746−2755.
(24) Cialla-May, D.; Zheng, X.-S.; Weber, K.; Popp, J. Recent progress in surface-enhanced Raman spectroscopy for biological and biomedical applications: from cells to clinics. *Chem. Soc. Rev.* **2017**, *46*, 3945−3961.
(25) Li, J.-F.; Zhang, Y.-J.; Ding, S.-Y.; Panneerselvam, R.; Tian, Z.-Q. Core-shell nanoparticle-enhanced Raman spectroscopy. *Chem. Rev.* **2017**, *117*, 5002−5069.
(26) Zong, C.; Xu, M.; Xu, L.-J.; Wei, T.; Ma, X.; Zheng, X.-S.; Hu, R.; Ren, B. Surface-enhanced Raman spectroscopy for bioanalysis: reliability and challenges. *Chem. Rev.* **2018**, *118*, 4946−4980.
(27) Zeng, Y.; Ren, J.; Shen, A.; Hu, J. Splicing nanoparticles-based "Click" SERS could aid multiplex liquid biopsy and accurate cellular imaging. *J. Am. Chem. Soc.* **2018**, *140*, 10649−10652.
(28) Pérez-Jiménez, A. I.; Lyu, D.; Lu, Z.; Liu, G.; Ren, B. Surface-enhanced Raman spectroscopy: benefits, trade-offs and future developments. *Chem. Sci.* **2020**, *11*, 4563−4577.
(29) Verma, P. Tip-enhanced Raman spectroscopy: technique and recent advances. *Chem. Rev.* **2017**, *117*, 6447−6466.
(30) Zhang, W.; Fang, Z.; Zhu, X. Near-field Raman spectroscopy with aperture tips. *Chem. Rev.* **2017**, *117*, 5095−5109.
(31) Pozzi, E. A.; Goubert, G.; Chiang, N.; Jiang, N.; Chapman, C. T.; McAnally, M. O.; Henry, A.-I.; Seideman, T.; Schatz, G. C.; Hersam, M. C.; Duyne, R. P. V. Ultrahigh-vacuum tip-enhanced Raman spectroscopy. *Chem. Rev.* **2017**, *117*, 4961−4982.
(32) Huang, Y.; Huang, S.; Wang, X.; Bodappa, N.; Li, C.; Yin, H.; Su, H.; Meng, M.; Zhang, H.; Ren, B.; Yang, Z.; Zenobi, R.; Tian, Z.; Li, J. Shell-isolated tip-enhanced Raman and fluorescence spectroscopy. *Angew. Chem., Int. Ed.* **2018**, *57*, 7523−7527.
(33) Su, H.; Feng, H.; Zhao, Q.; Zhang, X.; Sun, J.; He, Y.; Huang, S.; Huang, T.; Zhong, J.; Wu, D.; Ren, B. Probing the local generation and diffusion of active oxygen species on a Pd/Au bimetallic surface by tip-enhanced Raman spectroscopy. *J. Am. Chem. Soc.* **2020**, *142* (3), 1341−1347.
(34) Yamakoshi, H.; Dodo, K.; Okada, M.; Ando, J.; Palonpon, A.; Fujita, K.; Kawata, S.; Sodeoka, M. Imaging of EdU, an alkyne-tagged cell proliferation probe, by Raman microscopy. *J. Am. Chem. Soc.* **2011**, *133*, 6102−6105.
(35) Yamakoshi, H.; Dodo, K.; Palonpon, A.; Ando, J.; Fujita, K.; Kawata, S.; Sodeoka, M. Alkyne-tag Raman imaging for visualization of mobile small molecules in live cells. *J. Am. Chem. Soc.* **2012**, *134*, 20681−20689.
(36) Hong, S.; Chen, T.; Zhu, Y.; Li, A.; Huang, Y.; Chen, X. Live-cell stimulated Raman scattering imaging of alkyne-tagged biomolecules. *Angew. Chem.* **2014**, *126*, 5937−5941.
(37) Song, Z.-L.; Chen, Z.; Bian, X.; Zhou, L. Y.; Ding, D.; Liang, H.; Zou, Y.-X.; Wang, S.-S.; Chen, L.; Yang, C.; Zhang, X.-B.; Tan, W. Alkyne-functionalized superstable graphitic silver nanoparticles for Raman imaging. *J. Am. Chem. Soc.* **2014**, *136*, 13558−13561.
(38) Wei, L.; Hu, F.; Shen, Y.; Chen, Z.; Yu, Y.; Lin, C.-C.; Wang, M. C; Min, W. Live-cell imaging of alkyne-tagged small biomolecules by stimulated Raman scattering. *Nat. Methods* **2014**, *11*, 410−412.
(39) Ando, J.; Asanuma, M.; Dodo, K.; Yamakoshi, H.; Kawata, S.; Fujita, K.; Sodeoka, M. Alkyne-tag SERS screening and identification of small-molecule-binding sites in protein. *J. Am. Chem. Soc.* **2016**, *138*, 13901−13910.
(40) Li, S.; Chen, T.; Wang, Y.; Liu, L.; Lv, F.; Li, Z.; Huang, Y.; Schanze, K. S.; Wang, S. Conjugated polymer with intrinsic alkyne units for synergistically enhanced Raman imaging in living cells. *Angew. Chem., Int. Ed.* **2017**, *56*, 13455−13458.
(41) Tian, S.; Li, H.; Li, Z.; Tang, H.; Yin, M.; Chen, Y.; Wang, S.; Gao, Y.; Yang, X.; Meng, F.; Lauher, J. W.; Wang, P.; Luo, L. Polydiacetylene-based ultrastrong bioorthogonal Raman probes for targeted live-cell Raman imaging. *Nat. Commun.* **2020**, *11*, 81.
(42) Li, Y.; Heo, J.; Lim, C.-K.; Pliss, A.; Kachynski, A. V.; Kuzmin, A. N.; Kim, S.; Prasad, P. N. Organelle specific imaging in live cells and immuno-labeling using resonance Raman probe. *Biomaterials* **2015**, *53*, 25−31.
(43) Kuzmin, A. N.; Pliss, A.; Lim, C.-K.; Heo, J.; Kim, S.; Rzhevskii, A.; Gu, B.; Yong, K.-T.; Wen, S.; Prasad, P. N. Resonance Raman probes for organelle-specific labeling in live cells. *Sci. Rep.* **2016**, *6*, 1−9.
(44) Wei, L.; Min, W. Electronic preresonance stimulated Raman scattering microscopy. *J. Phys. Chem. Lett.* **2018**, *9*, 4294−4301.
(45) Bandara, H. D.; Burdette, S. C. Photoisomerization in different classes of azobenzene. *Chem. Soc. Rev.* **2012**, *41*, 1809−1825.
(46) Dong, M.; Babalhavaeji, A.; Samanta, S.; Beharry, A. A.; Woolley, G. A. Red-shifting azobenzene photoswitches for in vivo use. *Acc. Chem. Res.* **2015**, *48*, 2662−2670.
(47) Chevalier, A.; Renard, P. Y.; Romieu, A. Azo-based fluorogenic probes for biosensing and bioimaging: recent advances and upcoming challenges. *Chem. - Asian J.* **2017**, *12*, 2008−2028.
(48) Ying, Y.; Li, Z.; Hu, Z.; Zhang, J.; Meng, F.; Cao, C.; Long, Y.; Tian, H. A Time-resolved single-molecular train based on aerolysin nanopore. *Chem.* **2018**, *4*, 1893−1901.
(49) Hu, Z.; Li, Z.; Ying, Y.; Zhang, J.; Cao, C.; Long, Y.; Tian, H. Real-time and accurate identification of single oligonucleotide

https://doi.org/10.1021/acscentsci.1c00117
ACS Cent. Sci. 2021, 7, 768−780

photoisomers via an aerolysin nanopore. *Anal. Chem.* **2018**, *90*, 4268−4272.
(50) Wei, T.; Lu, S.; Sun, J.; Xu, Z.; Yang, X.; Wang, F.; Ma, Y.; Shi, Y. S.; Chen, X. Sanger's Reagent Sensitized Photocleavage of Amide Bond for Constructing Photocages and Regulation of Biological Functions. *J. Am. Chem. Soc.* **2020**, *142*, 3806−3813.
(51) Krutzik, P. O.; Nolan, G. P. Fluorescent cell barcoding in flow cytometry allows high-throughput drug screening and signaling profiling. *Nat. Methods* **2006**, *3*, 361−368.
(52) Livet, J.; Weissman, T. A.; Kang, H.; Draft, R. W.; Lu, J.; Bennis, R. A.; Sanes, J. R.; Lichtman, J. W. Transgenic strategies for combinatorial expression of fluorescent proteins in the nervous system. *Nature* **2007**, *450*, 56−63.
(53) Weber, K.; Thomaschewski, M.; Warlich, M.; Volz, T.; Cornils, K.; Niebuhr, B.; Täger, M.; Lütgehetmann, M.; Pollok, J.; Stocking, C.; Dandri, M.; Benten, D.; Fehse, B. RGB marking facilitates multicolor clonal cell tracking. *Nat. Med.* **2011**, *17*, 504−510.
(54) Cai, D.; Cohen, K. B.; Luo, T.; Lichtman, J. W.; Sanes, J. R. Improved tools for the Brainbow toolbox. *Nat. Methods* **2013**, *10*, 540−549.
(55) Giudice, V.; Feng, X.; Kajigaya, S.; Young, N. S.; Biancotto, A. Optimization and standardization of fluorescent cell barcoding for multiplexed flow cytometric phenotyping. *Cytometry, Part A* **2017**, *91*, 694−703.
(56) Boelens, H. F.M.; Dijkstra, R. J.; Eilers, P. H.C.; Fitzpatrick, F.; Westerhuis, J. A. New background correction method for liquid chromatography with diode array detection, infrared spectroscopic detection and Raman spectroscopic detection. *J. Chromatogr. A* **2004**, *1057*, 21−30.
(57) Liu, G.; Dong, F.; Fu, C.; Smith, Z. J. Automated morphometry toolbox for analysis of microscopic model organisms using simple bright-field imaging. *Biol. Open* **2019**, *8*, No. bio037788.
(58) Nascimento, J. M. P.; Dias, J. M. B. Vertex component analysis: a fast algorithm to unmix hyperspectral data. *IEEE Trans. Geosci. Remote Sens.* **2005**, *43*, 898−910.

https://doi.org/10.1021/acscentsci.1c00117
ACS Cent. Sci. 2021, 7, 768−780